

Probing protein orientation near charged surfaces with an implicit-solvent model and the PyGBe code

Christopher D. Cooper^{1, a)} and Lorena A. Barba^{2, b)}

¹⁾*Department of Mechanical Engineering, Boston University, Boston, MA.^{c)}*

²⁾*Department of Mechanical & Aerospace Engineering, The George Washington University, Washington, DC.*

(Dated: 27 March 2025)

Protein-surface interactions are ubiquitous in biological processes and bioengineering, yet are not fully understood. In the field of biosensors, a key factor in biosensor performance is the orientation of biomolecules near charged surfaces. The aim of this work is developing and assessing a computational model to study proteins interacting with charged surfaces and obtain orientation data. After extending the implicit-solvent model used in the open-source code **PyGBe** and deriving an analytical solution for simple geometry, our careful grid-convergence analysis builds confidence on the correctness and value of our approach for probing protein orientation. Further computational experiments support it: they study preferred orientations for protein GB1 D4' and immunoglobulin G. Sampling the free energy for protein GB1 at a range of tilt and rotation angles with respect to the charged surface, we calculated the probability of the protein orientation and observed a dipolar behavior. This result is consistent with published molecular-dynamics simulations and experimental studies using this protein. The case of immunoglobulin G is more challenging due to the large size of the molecule, but it is also more relevant to biosensor technology. The probability distribution of orientations for this protein at varying surface charge and salt concentration suggests that it is easier to control the antibody orientation with low salt concentration and high surface charge. The results also show that local interactions dominate over dipole moment for this protein. In view of its capacity to deal with much larger biomolecules than direct simulation, this implicit-solvent model can offer a valuable approach in biosensor studies.

I. INTRODUCTION

Proteins interacting with surfaces and adsorption mechanisms are ubiquitous and play a role in many biological processes. Along its importance in natural activity, like blood coagulation, adsorption affects biotechnologies like tissue engineering, biomedical implants and biosensors. Yet, despite their importance, a full understanding of protein-surface interactions remains elusive.^{1,2}

In the field of biosensors, protein adsorption needs to be engineered to obtain a successful device. Biosensors detect specific molecules using a nanoscale sensing element, like a metallic nanoparticle or nanowire covered with a bioactive coating. The prevalent way to modify a sensor surface is via a self-assembled monolayer (SAM) of a small charged group, with ligand molecules layered on top to achieve the desired function. Antibodies are a common choice for the ligand molecules, although the newest devices use single-domain or single-chain fragment molecules.^{3,4} Sensing occurs when a target biomolecule binds to the ligand molecule, changing some physical parameter on the sensor, such as current in nanowires or plasmon resonance frequency in metallic nanoparticles.

One of the factors affecting biosensor performance is the orientation of ligand molecules.^{5,6} These have specific binding sites, which need to be accessible to the target molecule for the biosensor to function well. Probing protein orientation is thus one key goal of adsorption studies. The aim of this study is to develop and assess a computational model to simulate proteins near surfaces and obtain orientation data.

We use an implicit-solvent approach based on the Poisson-Boltzmann equation and fixed protein structures. A sensor element, functionalized with the SAM, can be represented as a charged surface that interacts electrostatically with a biomolecule. Ignoring conformational changes of the biomolecule is justified in this application, since binding sites should remain nearly unmodified during the fabrication process.⁵

Implicit-solvent models using the Poisson-Boltzmann equation are popular for computing solvation energies in protein systems,^{7,8} but few studies have included the effect of surfaces. Lenhoff and co-workers studied surface-protein interactions using continuum models discretized with boundary-element^{9–11} and finite-difference methods,^{12,13} in the context of ion-exchange chromatography. They realized that van der Waals effects can be neglected for realistic molecular geometries¹⁴ and that the model is adequate as long as conformational changes in the protein are slight.^{12,13}

As far as we know, the continuum framework has not been used or assessed in the context of protein-orientation studies. One such study used a coarse-grained model of the molecule, represented as a set of spheres,^{15,16} and others assigned effective charges at the

^{a)}cdcooper@bu.edu

^{b)}labarba@gwu.edu

^{c)}New address: Department of Mechanical Engineering, Universidad Técnica Federico Santa María, Valparaíso, Chile.

residue level,^{17,18} or made approximations to account for pH effects.^{19,20}

We have added the capability of modeling a protein near a charged surface to our code PyGBe, an open-source code²¹ that uses GPU hardware. Previously, we verified and validated PyGBe in its use to obtain solvation and binding energies, by comparing with analytical solutions of the equations and with results obtained using the well-known APBS software.^{22,23} In the present work, we derived an analytical solution for a spherical molecule interacting with a spherical charged surface, and used it to verify the code in its new application and study numerical convergence. Using the newly extended code, we studied two proteins (GB1 D4' and immunoglobulin-G) near charged surfaces to obtain their preferred orientation, and compared ours and several other published results. We anticipate this modeling tool to be useful for understanding the behavior of proteins as they adsorb on SAMs, potentially aiding the design of better ligand molecules for biosensors.

II. IMPLICIT-SOLVENT MODEL FOR PROTEINS NEAR CHARGED SURFACES

The implicit-solvent model uses continuum electrostatics to describe the mean-field potential in a molecular system. A typical system consists of a protein in a solvent, defining two regions: inside and outside the protein, with an interface marked by the solvent-excluded surface (SES). The SES, beyond which a water molecule cannot penetrate into the protein, can be generated by rolling a (virtual) spherical probe of the size of a water molecule around the protein (see Figure 1). Inside the protein, the domain has low permittivity ($\epsilon = 2$ to 4) and there are point charges located at the positions of the atoms. The solvent region, representing water with salt, has a permittivity of $\epsilon \approx 80$. A system of partial differential equations models this situation, with a Poisson equation governing inside the protein and a linearized Poisson-Boltzmann equation governing in the solvent region. Appropriate interface conditions on the SES express the continuity of the potential and electric displacement, completing the mathematical formulation.

This model has been widely applied to investigate interactions between molecules, such as in protein-ligand binding. We are interested here in an extension of the model to consider interactions between proteins and surfaces with an imposed potential or charge. This new setup is sketched in Figure 2, and is described mathematically by the following equations:

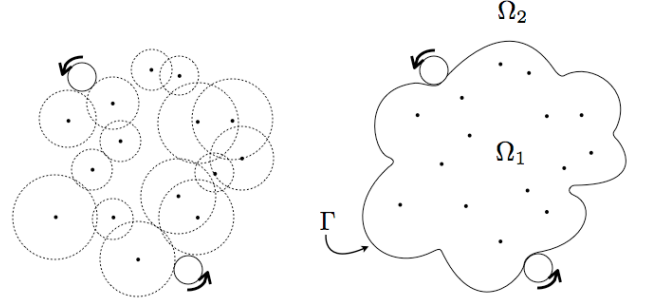


FIG. 1: Sketch of the process for generating a solvent-excluded surface (SES): a protein molecule contains a set of atoms that define a radius upon applying a force field and a probe the size of a water molecule is rolled to define the SES. Ω_1 is the protein region and Ω_2 the solvent region.

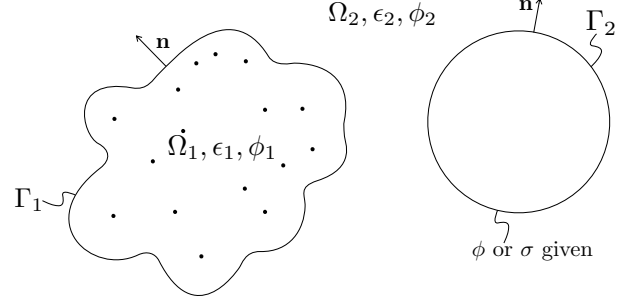


FIG. 2: Sketch of a molecule interacting with a surface: Ω_1 is the protein, Ω_2 the solvent region, Γ_1 is the SES and Γ_2 a nanosurface with imposed charge or potential.

$$\begin{aligned}
 \nabla^2 \phi_1(\mathbf{r}) &= - \sum_k \frac{q_k}{\epsilon_1} \delta(\mathbf{r}, \mathbf{r}_k) \quad \text{in solute } (\Omega_1), \\
 \nabla^2 \phi_2(\mathbf{r}) &= \kappa^2 \phi_2(\mathbf{r}) \quad \text{in solvent } (\Omega_2), \\
 \phi_1 &= \phi_2 \quad \text{on interface } \Gamma_1, \\
 \epsilon_1 \frac{\partial \phi_1}{\partial \mathbf{n}} &= \epsilon_2 \frac{\partial \phi_2}{\partial \mathbf{n}} \\
 \phi_2 &= \phi_0 \text{ or } -\epsilon_2 \frac{\partial \phi_2}{\partial \mathbf{n}} = \sigma_0 \quad \text{on surface } \Gamma_2, \quad (1)
 \end{aligned}$$

Here, ϕ_i is the potential corresponding to the region Ω_i with permittivity ϵ_i , and ϕ_0 and σ_0 are the set potential or charge on the nanosurface. The surface Γ_2 could correspond to a device such as a biosensor.

Boundary integral formulation— We express the system of partial-differential equations in (1) by the corresponding integral equations along the interface and the nanosurface, Γ_1 and Γ_2 . Many authors have used the boundary-integral representation of the implicit-solvent model to compute solvation energies of proteins,^{23–29} but apart from work led by Lenhoff,⁹ we know of no studies that account for interacting nanosurfaces in the system.

Consider the setting in Figure 2 with prescribed potential at Γ_2 . The application of Green's second identity on the first two equations of (1) yields:

$$\begin{aligned} \phi_1 + K_L^{\Omega_1}(\phi_{1,\Gamma_1}) - V_L^{\Omega_1} \left(\frac{\partial}{\partial \mathbf{n}} \phi_{1,\Gamma_1} \right) &= \\ \frac{1}{\epsilon_1} \sum_{k=0}^{N_q} \frac{q_k}{4\pi |\mathbf{r}_{\Omega_1} - \mathbf{r}_k|} &\quad \text{on } \Omega_1, \\ \phi_2 - K_Y^{\Omega_2}(\phi_{2,\Gamma_1}) + V_Y^{\Omega_2} \left(\frac{\partial}{\partial \mathbf{n}} \phi_{2,\Gamma_1} \right) - K_Y^{\Omega_2}(\phi_{2,\Gamma_2}) &+ V_Y^{\Omega_2} \left(\frac{\partial}{\partial \mathbf{n}} \phi_{2,\Gamma_2} \right) = 0 \quad \text{on } \Omega_2, \end{aligned} \quad (2)$$

where $\phi_{i,\Gamma_j} = \phi_i(\mathbf{r}_{\Gamma_j})$ is the potential in region Ω_i evaluated at the surface Γ_j . K and V are defined as

$$\begin{aligned} K_{L/Y}^{\Omega_i}(\phi_{i,\Gamma_j}) &= \oint_{\Gamma_j} \frac{\partial}{\partial \mathbf{n}} [G_{L/Y}(\mathbf{r}_{\Omega_i}, \mathbf{r}_{\Gamma_j})] \phi_{i,\Gamma_j} d\Gamma, \\ V_{L/Y}^{\Omega_i} \left(\frac{\partial}{\partial \mathbf{n}} \phi_{i,\Gamma_j} \right) &= \oint_{\Gamma_j} \frac{\partial}{\partial \mathbf{n}} \phi_{i,\Gamma_j} G_{L/Y}(\mathbf{r}_{\Omega_i}, \mathbf{r}_{\Gamma_j}) d\Gamma, \end{aligned} \quad (3)$$

corresponding to the double- and single-layer potentials of ϕ_{i,Γ_j} and $\frac{\partial}{\partial \mathbf{n}} \phi_{i,\Gamma_j}$ evaluated in the region Ω_i . The functions G_L and G_Y are the free-space Green's functions of the Poisson (Laplace kernel) and linearized Poisson-Boltzmann (Yukawa kernel) equations, respectively:

$$\begin{aligned} G_L(\mathbf{r}_{\Omega_1}, \mathbf{r}_{\Gamma_1}) &= \frac{1}{4\pi |\mathbf{r}_{\Omega_1} - \mathbf{r}_{\Gamma_1}|}, \\ G_Y(\mathbf{r}_{\Omega_2}, \mathbf{r}_{\Gamma_2}) &= \frac{\exp(-\kappa |\mathbf{r}_{\Omega_2} - \mathbf{r}_{\Gamma_2}|)}{4\pi |\mathbf{r}_{\Omega_2} - \mathbf{r}_{\Gamma_2}|}. \end{aligned} \quad (4)$$

We then take the limits $\mathbf{r}_{\Omega_1} \rightarrow \mathbf{r}_{\Gamma_1}$, $\mathbf{r}_{\Omega_2} \rightarrow \mathbf{r}_{\Gamma_1}$, $\mathbf{r}_{\Omega_2} \rightarrow \mathbf{r}_{\Gamma_2}$ on Equation (2), and apply the boundary conditions: $\phi_{1,\Gamma_1} = \phi_{2,\Gamma_1}$, $\epsilon_1 \frac{\partial}{\partial \mathbf{n}} \phi_{1,\Gamma_1} = \epsilon_2 \frac{\partial}{\partial \mathbf{n}} \phi_{2,\Gamma_1}$ and $\phi_{2,\Gamma_2} = \phi_0$ to get the following system of boundary equations:

$$\begin{aligned} \frac{\phi_{1,\Gamma_1}}{2} + K_L^{\Gamma_1}(\phi_{1,\Gamma_1}) - V_L^{\Gamma_1} \left(\frac{\partial}{\partial \mathbf{n}} \phi_{1,\Gamma_1} \right) &= \frac{1}{\epsilon_1} \sum_{k=0}^{N_q} \frac{q_k}{4\pi |\mathbf{r}_{\Gamma_1} - \mathbf{r}_k|} \quad \text{on } \Gamma_1, \\ \frac{\phi_{1,\Gamma_1}}{2} - K_Y^{\Gamma_1}(\phi_{1,\Gamma_1}) + \frac{\epsilon_1}{\epsilon_2} V_Y^{\Gamma_1} \left(\frac{\partial}{\partial \mathbf{n}} \phi_{1,\Gamma_1} \right) - K_Y^{\Gamma_1}(\phi_0) + V_Y^{\Gamma_1} \left(\frac{\partial}{\partial \mathbf{n}} \phi_{2,\Gamma_2} \right) &= 0 \quad \text{on } \Gamma_1, \\ -K_Y^{\Gamma_2}(\phi_{1,\Gamma_1}) + \frac{\epsilon_1}{\epsilon_2} V_Y^{\Gamma_2} \left(\frac{\partial}{\partial \mathbf{n}} \phi_{1,\Gamma_1} \right) + \frac{\phi_0}{2} - K_Y^{\Gamma_2}(\phi_0) + V_Y^{\Gamma_2} \left(\frac{\partial}{\partial \mathbf{n}} \phi_{2,\Gamma_2} \right) &= 0 \quad \text{on } \Gamma_2. \end{aligned} \quad (5)$$

Rearranging terms, we write Equation (5) in matrix form, as follows:

$$\begin{bmatrix} \frac{1}{2} + K_L^{\Gamma_1} & -V_L^{\Gamma_1} & 0 \\ \frac{1}{2} - K_Y^{\Gamma_1} & \frac{\epsilon_1}{\epsilon_2} V_Y^{\Gamma_1} & V_Y^{\Gamma_1} \\ -K_Y^{\Gamma_2} & \frac{\epsilon_1}{\epsilon_2} V_Y^{\Gamma_2} & V_Y^{\Gamma_2} \end{bmatrix} \begin{bmatrix} \phi_{1,\Gamma_1} \\ \frac{\partial}{\partial \mathbf{n}} \phi_{1,\Gamma_1} \\ \frac{\partial}{\partial \mathbf{n}} \phi_{2,\Gamma_2} \end{bmatrix} = \begin{bmatrix} \sum_{k=0}^{N_q} \frac{q_k}{4\pi |\mathbf{r}_{\Gamma_1} - \mathbf{r}_k|} \\ K_Y^{\Gamma_1}(\phi_0) \\ -\left(\frac{1}{2} - K_Y^{\Gamma_2}\right)(\phi_0) \end{bmatrix}. \quad (6)$$

If the surface Γ_2 has prescribed charge, corresponding to a Neumann boundary condition, $-\epsilon_2 \frac{\partial}{\partial \mathbf{n}} \phi_{2,\Gamma_2} = \sigma_0$, the equivalent derivation yields

$$\begin{bmatrix} \frac{1}{2} + K_L^{\Gamma_1} & -V_L^{\Gamma_1} & 0 \\ \frac{1}{2} - K_Y^{\Gamma_1} & \frac{\epsilon_1}{\epsilon_2} V_Y^{\Gamma_1} & -K_Y^{\Gamma_1} \\ -K_Y^{\Gamma_2} & \frac{\epsilon_1}{\epsilon_2} V_Y^{\Gamma_2} & \left(\frac{1}{2} - K_Y^{\Gamma_2}\right) \end{bmatrix} \begin{bmatrix} \phi_{1,\Gamma_1} \\ \frac{\partial}{\partial \mathbf{n}} \phi_{1,\Gamma_1} \\ \phi_{2,\Gamma_2} \end{bmatrix} = \begin{bmatrix} \sum_{k=0}^{N_q} \frac{q_k}{4\pi |\mathbf{r}_{\Gamma_1} - \mathbf{r}_k|} \\ -V_Y^{\Gamma_1} \left(\frac{\partial}{\partial \mathbf{n}} \phi_{2,\Gamma_2} \right) \\ -V_Y^{\Gamma_2} \left(\frac{\partial}{\partial \mathbf{n}} \phi_{2,\Gamma_2} \right) \end{bmatrix}. \quad (7)$$

The formulation detailed in this section differs from the work by Lenhoff and co-workers^{9,10} because they consider an infinite charged surface, modeled using a modified Green's function to account for the half-space domain. Lenhoff's approach has the advantage that the charged surface does not require a mesh, but presents difficulties if the surface has a complex geometry. More-

over, an infinite surface may not be a good model if its size is comparable to the protein's, like it happens with nano-structures.

This formulation can be extended to account for Stern layers and solvent-filled cavities, by adding more surfaces or interfaces. In our code, we deal with multiple surfaces in the manner presented by Altman and co-workers,²⁸ as described in our previous paper.²³

III. METHODS

A. Discretization

To numerically solve the system in (5), we discretize the boundaries into flat triangular panels and assume that ϕ and $\frac{\partial\phi}{\partial\mathbf{n}}$ are constant within those panels. The discretized form of the integral operators is as follows:

$$\begin{aligned} K_{L,\text{disc}}^{\mathbf{r}_i}(\phi(\mathbf{r}_\Gamma)) &= \sum_{j=1}^{N_p} \phi(\mathbf{r}_{\Gamma_j}) \int_{\Gamma_j} \frac{\partial}{\partial\mathbf{n}} [G_L(\mathbf{r}_i, \mathbf{r}_{\Gamma_j})] d\Gamma_j, \\ V_{L,\text{disc}}^{\mathbf{r}_i} \left(\frac{\partial}{\partial\mathbf{n}} \phi(\mathbf{r}_\Gamma) \right) &= \sum_{j=1}^{N_p} \frac{\partial}{\partial\mathbf{n}} \phi(\mathbf{r}_{\Gamma_j}) \int_{\Gamma_j} G_L(\mathbf{r}_i, \mathbf{r}_{\Gamma_j}) d\Gamma_j, \end{aligned} \quad (8)$$

where N_p is the number of discretization elements on Γ , and $\phi(\mathbf{r}_{\Gamma_j})$ and $\frac{\partial}{\partial\mathbf{n}} \phi(\mathbf{r}_{\Gamma_j})$ are the constant values of ϕ and $\frac{\partial\phi}{\partial\mathbf{n}}$ on panel Γ_j (we are somewhat abusing the nomenclature here by reusing the symbol Γ , which previously referred to the complete surface). By collocating \mathbf{r}_i on the center of each panel, we get a linear system of equations which looks just like those in Equations (6) and (7), but its elements are sub-matrices of size $N_p \times N_p$ rather than integral operators. Looking at Figure 3, each element of a sub-matrix is an integral over one panel Γ_j ,

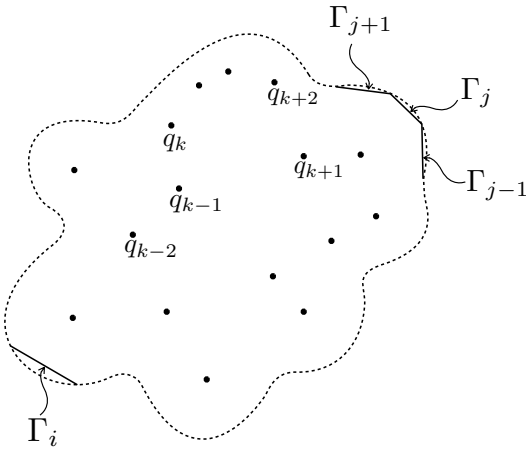


FIG. 3: Discretization of a molecular surface. Γ_i is the panel where the collocation point resides and Γ_j the panel being integrated.

with \mathbf{r}_i located at the center of the collocation panel Γ_i , as follows:

$$\begin{aligned} K_{L,ij} &= \int_{\Gamma_j} \frac{\partial}{\partial\mathbf{n}} [G_L(\mathbf{r}_{\Gamma_i}, \mathbf{r}_{\Gamma_j})] d\Gamma_j, \\ V_{L,ij} &= \int_{\Gamma_j} G_L(\mathbf{r}_{\Gamma_i}, \mathbf{r}_{\Gamma_j}) d\Gamma_j. \end{aligned} \quad (9)$$

The terms on the right-hand side and the unknown vectors in the discretized form of Equation (6) are sub-vectors of size N_p . In this case, each element is the evaluation on the collocation panel Γ_i , written as

$$\begin{aligned} \phi_{1,\Gamma_1} &= \phi_1(\mathbf{r}_i), \\ \frac{\partial}{\partial\mathbf{n}} \phi_{1,\Gamma_1} &= \frac{\partial}{\partial\mathbf{n}} \phi_1(\mathbf{r}_i), \\ \sum_{k=0}^{N_q} \frac{q}{4\pi|\mathbf{r}_{\Gamma_1} - \mathbf{r}_k|} &= \sum_{k=0}^{N_q} \frac{q}{4\pi|\mathbf{r}_i - \mathbf{r}_k|}, \end{aligned} \quad (10)$$

where \mathbf{r}_i is located at the center of panel Γ_i .

In our numerical solution, integrals are calculated in three ways, depending on how close the panel is to the collocation point. When the collocation point is inside the element being integrated, we use a semi-analytical technique,³⁰ with Gauss points placed along the edges of the element. If the integrated element is closer than $2L$ from the collocation point —where $L = \sqrt{2 \cdot \text{Area}}$ — we use a fine Gauss quadrature rule, with 19 or more points per element. Beyond a distance of $2L$, elements have only 1, 3, 4 or 7 Gauss points, depending on the case.

B. Treecode-accelerated boundary element method

Most modern implementations of the boundary element method (BEM) use Krylov methods to solve the linear system, usually a general minimal residual method (GMRES), which is agnostic to the structure of the matrix. In practice, Krylov solvers for BEM require $O(n \cdot N_p^2)$ operations to obtain the unknown vector, where n is the number of iterations to get a desired residual, and is much smaller than N_p . The $O(N^2)$ scaling is given by a matrix-vector product (with a dense matrix) done in every iteration; this is the most time-consuming part of the algorithm, and makes BEM prohibitive for more than a few thousand discretization elements.

But when we inspect the approximation of the integrals in (9) with Gauss quadrature rules, we see that the matrix-vector product has the form of an N -body problem, similar to gravitational potential calculations in planetary systems. In this case, the Gauss quadrature points act analogously to planets (sources of mass) and the collocation points are analogous to the locations where the gravitational potential is computed (targets points). There are several ways to accelerate this kind of computations, for example fast-multipole methods,³¹

treecodes,³² and fast-Fourier-transform methods.³³ In our numerical solution (developed as the open-source code **PyGBe**), we accelerate the N -body calculation with a treecode,^{32,34} making this part of the algorithm scale as $O(N \log N)$ rather than $O(N^2)$.

The treecode algorithm groups the sources and targets in a tree-structured set of boxes and approximates interactions between far-away boxes using a series expansion—a Taylor series, in our case. This allows for controllable accuracy that depends on the number of terms used in the expansion and the multipole-acceptance criterion that defines the threshold where the distance between source and target is far enough to approximate the interactions with expansions. Details of our implementation of the treecode in **PyGBe** can be found in our previous work.²²

C. Energy calculation

Figure 2 shows an arrangement with three types of free energy: Coulombic energy from the point charges, surface energy due to Γ_2 and solvation energy. The Coulombic energy arises simply from the Coulomb interactions of all point charges. This section describes how we compute the other two components of free energy in the boundary-element framework.

Solvation free energy— When a protein is in a solvated state, surrounded by water molecules that have become polarized, its free energy differs from its state *in vacuo* by an amount known as the solvation energy. Its free energy again differs in the presence of other structures in the solvent, e.g., other proteins or charged surfaces. In this work we use the term solvation energy to more broadly mean the change in free energy of the protein from its state in a vacuum, to its state in the solvent with any other components or structures. In single-molecule settings, this definition of solvation energy coincides with the energy required to solvate the molecule.

To calculate the solvation energy, the total minus the Coulomb potential is applied inside the protein, i.e.,

$$F_{\text{solv}} = \frac{1}{2} \int_{\Omega} \rho (\phi_{\text{total}} - \phi_{\text{Coulomb}}) \quad (11)$$

$$= \sum_{k=0}^{N_q} q_k (\phi_{\text{total}} - \phi_{\text{Coulomb}})(\mathbf{r}_k), \quad (12)$$

where ρ is the charge distribution, consisting of point charges (which transforms the integral into a sum). The total minus Coulomb potential includes the reaction potential—representing the response of the solvent by polarization and rearrangement of free ions—and any effects from the immersed surface. We can also interpret it as the potential generated by the boundary Γ of the molecular region Ω . Taking the first expression of Equa-

tion (2) and subtracting out the Coulombic effect yields

$$\phi_{\text{reac}, \mathbf{r}_k} = -K_L^{\mathbf{r}_k}(\phi_{1, \Gamma_1}) + V_L^{\mathbf{r}_k} \left(\frac{\partial}{\partial \mathbf{n}} \phi_{1, \Gamma_1} \right) \quad (13)$$

Equation (11) requires evaluating ϕ_{reac} for each point-charge location \mathbf{r}_k . We obtain this by discretizing Equation (13) and using the solution of the linear system in Equation (6) or Equation (7) as inputs.

Surface free energy— Chan and co-workers^{35,36} derived the free energy for a surface with a set charge or potential. They describe the free energy on a surface as

$$F = \frac{1}{2} \int_{\Gamma} G_c \sigma_0^2 d\Gamma \quad \text{for set charge, and}$$

$$F = -\frac{1}{2} \int_{\Gamma} G_p \phi_0^2 d\Gamma \quad \text{for set potential,} \quad (14)$$

where ϕ_0 and σ_0 are the prescribed potential and surface charge, respectively. The potential is given by $\phi(\sigma, R, \mathbf{x}) = G_c(R, \mathbf{x})\sigma$ for the first expression and the surface charge by $\sigma(\phi, R, \mathbf{x}) = G_p(R, \mathbf{x})\phi$ for the second one. This is valid because we are using a linearized Poisson-Boltzmann model.

Using constant values of ϕ and $\frac{\partial \phi}{\partial \mathbf{n}}$ per panel, the discretized version of Equation (14) takes the form

$$F = \frac{1}{2} \sum_{j=1}^{N_p} \phi(\mathbf{r}_j) \sigma_{0j} A_j, \text{ and}$$

$$F = -\frac{1}{2} \sum_{j=1}^{N_p} \phi_{0j} \sigma(\mathbf{r}_j) A_j. \quad (15)$$

where A_j is the area of panel j , and $\sigma = \epsilon \frac{\partial \phi}{\partial \mathbf{n}}$. To obtain the surface free energy, we can plug in the solution of the system in Equation (6) or (7) to Equation (15).

Interaction free energy— When there are two or more bodies in the solvent, they will interact electrostatically. In order to compute the energy of interaction, we need to take the difference between the total energy of the interacting system and the total energy of each isolated component, where the total free energy is given by

$$F_{\text{total}} = F_{\text{Coulomb}} + F_{\text{surface}} + F_{\text{solv}}. \quad (16)$$

The interaction free energy is

$$F_{\text{interaction}} = F_{\text{total}}^{\text{assembly}} - \sum_{i=1}^{N_c} F_{\text{total}}^{\text{comp}_i}, \quad (17)$$

where N_c is the number of components in the system and $F_{\text{total}}^{\text{comp}_i}$ is calculated over the isolated component i .

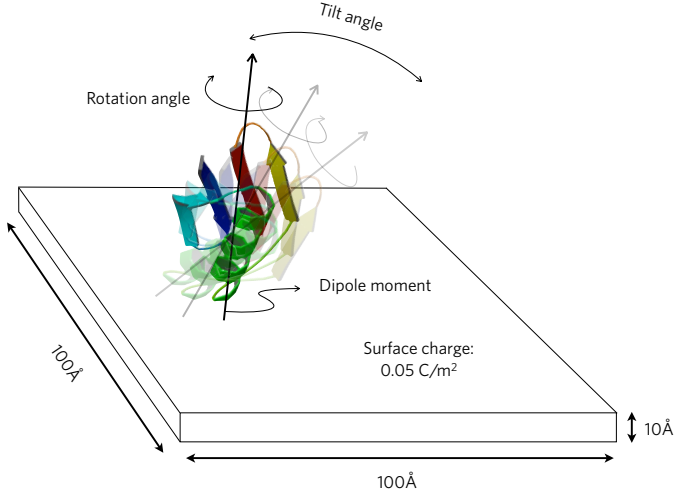


FIG. 4: Setup of orientation experiment.

D. Orientation sampling of a protein near a charged surface

We are interested in studying the orientation of proteins near self-assembled monolayers (SAM), specifically for biosensing applications. In the framework of the implicit-solvent model, we can represent the SAM as a surface charge density, and use Equation (7) to compute the electrostatic potential. According to the Boltzmann distribution, the probability of finding the system in micro-state λ depends on the total free energy, F_{total} , as

$$P(\lambda) = \frac{\int_{\lambda} \exp\left(-\frac{F_{\text{total}}}{k_B T}\right) d\lambda}{\int_{\Lambda} \exp\left(-\frac{F_{\text{total}}}{k_B T}\right) d\Lambda}, \quad (18)$$

where Λ is the ensemble of all micro-states, k_B the Boltzmann constant and T the temperature. To obtain a probability distribution, we used Equation (18) assuming that electrostatic effects were dominant, and sampled F_{total} for different orientations. We defined the orientation using the angle between the dipole moment and surface normal vectors as a reference (tilt angle), varying from 0° to 180° . Also, for each tilt angle, we rotated the protein about the dipole moment vector in 360° to examine all possible orientations. This process is sketched in Figure 4.

In this case, micro-states are defined by the tilt (α_{tilt}) and rotational (α_{rot}) angles, and we rewrite the integral in the numerator of Equation (18) as

$$\int_{\lambda} \exp\left(-\frac{F_{\text{total}}}{k_B T}\right) d\lambda = \int \int \exp\left(-\frac{F_{\text{total}}}{k_B T}\right) d\alpha_{\text{rot}} d\alpha_{\text{tilt}}, \quad (19)$$

where micro-state λ is a range of angles α_{rot} and α_{tilt} .

To assess the performance of the implicit solvent model for investigating protein-surface interactions, we studied the orientation of protein G B1 D4' mutant near

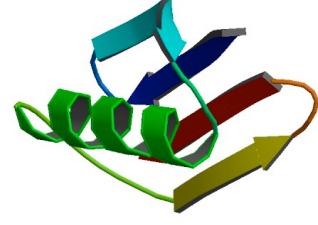


FIG. 5: Structure of Protein G B1 (PDB code: 1PGB).



FIG. 6: Structure of Immunoglobulin G (PDB code: 1IGT).

a charged surface, since there are molecular dynamics simulations³⁷ and experimental observations³⁸ available in the literature that we could compare to. Figure 5 shows the structure of Protein G B1 (PDB code 1PGB), to which we applied mutations E19Q, D22N, D46N and D47N to obtain the D4' mutant, using the SwissPdb Viewer software.^{39,40}

We carried out a similar study for the antibody immunoglobulin G (PDB code 1IGT), a widely used protein in biosensors, whose structure is shown in Figure 6. This is a more interesting case from the point of view of our application, yet we do not have the benefit of published simulations or experiments to compare to.

IV. ANALYTICAL SOLUTION

It is possible to derive a closed-form expression for the free energy of interaction between a spherical molecule with a centered charge and a spherical surface with imposed potential or charge, like the one sketched in Figure 7. There are such analytical expressions for interacting charged surfaces,⁴¹ and interacting spherical molecules with multiple point charges inside,⁴² but not for a situation where surfaces and molecules interact. Having such an analytical solution is of great utility in the de-

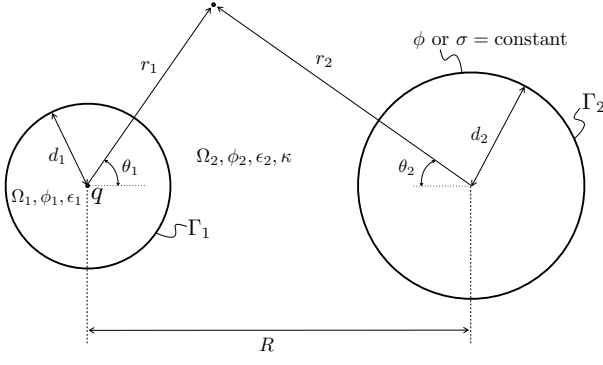


FIG. 7: Sketch of system solved with Legendre polynomials expansions.

velopment of a computational model for protein-surface interaction, because it will allow for proper code verification.

A. Expansion in Legendre polynomials

The system of partial differential equations from Equation (1) models the electrostatic potential field in the setting of Figure 7. Following Carnie and co-workers,⁴¹ the axial symmetry lets us formulate the solution of Equation (1) as an expansion in Legendre polynomials:

$$A_{nm}^\nu = \frac{\Gamma(n - \nu + 0.5)\Gamma(m - \nu + 0.5)\Gamma(\nu + 0.5)(n + m - \nu)!(n + m - 2\nu + 0.5)}{\pi\Gamma(m + n - \nu + 1.5)(n - \nu)!(m - \nu)!\nu!}. \quad (24)$$

Legendre polynomials are orthogonal to each other, and $\frac{q}{4\pi\epsilon_1 r_1}$ is independent of θ . Thus, taking the inner product of the expressions in Equations (20) and (22) with $P_j(\cos \theta_i)$, where $i = 1$ or 2 , yields

$$\phi_1 \delta_{0j} = c_j r_1^j + \frac{q}{4\pi\epsilon_1 r_1} \delta_{0j} \quad (25)$$

$$\begin{aligned} \phi_1 &= \sum_{n=0}^{\infty} c_n r_1^n P_n(\cos \theta_1) + \frac{q}{4\pi\epsilon_1 r_1} \quad \text{on } \Omega_1, \\ \phi_2 &= \sum_{n=0}^{\infty} a_n k_n(\kappa r_1) P_n(\cos \theta_1) \\ &\quad + \sum_{n=0}^{\infty} b_n k_n(\kappa r_2) P_n(\cos \theta_2) \quad \text{on } \Omega_2, \end{aligned} \quad (20)$$

being P_n the n^{th} -degree Legendre polynomial and k_n the modified spherical Bessel function of the second kind.

We make use of the following addition formula,⁴³

$$k_n(\kappa r_2) P_n(\cos \theta_2) = \sum_{m=0}^{\infty} (2m+1) B_{nm} i_m(\kappa r_1) P_m(\cos \theta_1), \quad (21)$$

to reformulate the expression for ϕ_2 in Equation (20) as

$$\begin{aligned} \phi_2 &= \sum_{n=0}^{\infty} a_n k_n(\kappa r_1) P_n(\cos \theta_1) \\ &\quad + \sum_{n=0}^{\infty} b_n \sum_{m=0}^{\infty} (2m+1) B_{nm} i_m(\kappa r_1) P_m(\cos \theta_1) \\ \phi_2 &= \sum_{n=0}^{\infty} b_n k_n(\kappa r_2) P_n(\cos \theta_2) \\ &\quad + \sum_{n=0}^{\infty} a_n \sum_{m=0}^{\infty} (2m+1) B_{nm} i_m(\kappa r_2) P_m(\cos \theta_2). \end{aligned} \quad (22)$$

Here, i_m is the modified spherical Bessel function of the first kind; B_{nm} is defined by

$$B_{nm} = \sum_{\nu=0}^{\infty} A_{nm}^\nu k_{n+m-2\nu}(\kappa R), \quad (23)$$

where R is the center-to-center distance; and A_{nm}^ν is given by the following expression, with Γ (in this context only) representing the gamma function:

for the first expression of Equation (20), and

$$\begin{aligned} \phi_2 \delta_{0j} &= a_j k_j(\kappa r_1) + \sum_{n=0}^{\infty} b_n (2j+1) B_{nj} i_j(\kappa r_1), \\ \phi_2 \delta_{0j} &= b_j k_j(\kappa r_2) + \sum_{n=0}^{\infty} a_n (2j+1) B_{nj} i_j(\kappa r_2) \end{aligned} \quad (26)$$

for Equation (22).

Applying the interface conditions for Γ_1 on Equation (25) and the first expression of Equation (26), produces

$$\sum_{n=0}^{\infty} a_n \left(\kappa k'_n(\kappa d_1) - \frac{\epsilon_1}{\epsilon_2} \frac{n}{d_1} k_n(\kappa d_1) \right) \delta_{nj} + b_n(2j+1)B_{nj} \left(\kappa i'_j(\kappa d_1) - \frac{\epsilon_1}{\epsilon_2} \frac{j}{d_1} i_j(\kappa d_1) \right) - \frac{\epsilon_1}{\epsilon_2} \frac{q}{4\pi\epsilon_1 d_1^2} \delta_{0j}(j+1), \quad (27)$$

where d_1 is the radius of surface 1.

Constant potential ϕ on Γ_2 .

The application of the boundary condition on Γ_2 , $\phi(\Gamma_2) = \phi_0$, where ϕ_0 is independent on θ_2 , gives

$$\sum_{n=0}^{\infty} a_n(2j+1)B_{nj}i_j(\kappa d_2) + b_n k_n(\kappa d_2)\delta_{nj} = \phi_0 \delta_{0j}. \quad (28)$$

Combining Equations (27) and (28) yields the following system of equations for the coefficients a_n and b_n

$$\begin{aligned} \mathbf{IA} + \mathbf{LB} &= -\frac{\epsilon_1}{\epsilon_2} \frac{q}{4\pi\epsilon_1 d_1^2} \mathbf{e} \\ \mathbf{MA} + \mathbf{IB} &= \phi_0 \mathbf{e} \end{aligned} \quad (29)$$

where

$$\begin{aligned} I_{jn} &= \delta_{jn} \\ e_j &= \delta_{0j} \\ A_n &= a_n \left(\kappa k'_n(\kappa d_1) - \frac{\epsilon_1}{\epsilon_2} \frac{n}{d_1} k_n(\kappa d_1) \right) \\ B_n &= b_n k_n(\kappa d_2) \\ L_{jn} &= (2j+1)B_{nj} \left(\kappa \frac{i'_j(\kappa d_1)}{k'_n(\kappa d_2)} - \frac{\epsilon_1}{\epsilon_2} \frac{j}{d_1} \frac{i_j(\kappa d_1)}{k_n(\kappa d_2)} \right) \\ M_{jn} &= (2j+1)B_{nj}i_j(\kappa d_2) \frac{1}{\left(\kappa k'_n(\kappa d_1) - \frac{\epsilon_1}{\epsilon_2} \frac{n}{d_1} k_n(\kappa d_1) \right)}. \end{aligned} \quad (30)$$

Constant surface charge σ on Γ_2 .

In this case, the application of the boundary condition on Γ_2 , $\sigma(\Gamma_2) = -\epsilon_2 \frac{\partial \phi}{\partial \mathbf{n}}|_{\Gamma_2} = \sigma_0$, where σ_0 is independent on θ_2 , gives

$$\sum_{n=0}^{\infty} a_n(2j+1)B_{nj}\kappa i'_j(\kappa d_2) + b_n \kappa k'_n(\kappa d_2)\delta_{nj} = -\frac{\sigma_0}{\epsilon_2} \delta_{0j} \quad (31)$$

Combining Equations (27) and (28) produces a system of equations for the coefficients a_n and b_n

$$\begin{aligned} \mathbf{IA} + \mathbf{LB} &= -\frac{\epsilon_1}{\epsilon_2} \frac{q}{4\pi\epsilon_1 d_1^2} \mathbf{e} \\ \mathbf{MA} + \mathbf{IB} &= -\frac{\sigma_0}{\epsilon_2} \mathbf{e} \end{aligned} \quad (32)$$

where

$$\begin{aligned} I_{jn} &= \delta_{jn} \\ e_j &= \delta_{0j} \\ A_n &= a_n \left(\kappa k'_n(\kappa d_1) - \frac{\epsilon_1}{\epsilon_2} \frac{n}{d_1} k_n(\kappa d_1) \right) \\ B_n &= b_n \kappa k'_n(\kappa d_2) \\ L_{jn} &= (2j+1)B_{nj} \left(\frac{i'_j(\kappa d_1)}{k'_n(\kappa d_2)} - \frac{\epsilon_1}{\epsilon_2} \frac{j}{d_1} \frac{i_j(\kappa d_1)}{\kappa k'_n(\kappa d_2)} \right) \\ M_{jn} &= (2j+1)B_{nj}\kappa i'_j(\kappa d_2) \frac{1}{\left(\kappa k'_n(\kappa d_1) - \frac{\epsilon_1}{\epsilon_2} \frac{n}{d_1} k_n(\kappa d_1) \right)}. \end{aligned} \quad (33)$$

B. Energy calculation

Solvation free energy of the molecule— According to Equation (11), the solvation free energy of a molecule with a centered charge is given by

$$F_{\text{solv}} = \frac{1}{2} q \phi_{\text{reac}}(r_1 = 0), \quad (34)$$

and using Equation (20), the reaction potential from Equation (13) is:

$$\phi_{\text{reac}} = \phi - \frac{q}{4\pi\epsilon_1 r} = \sum_{n=0}^{\infty} c_n r^n P_n(\cos \theta_1). \quad (35)$$

Applying the boundary conditions at Γ_1 on Equation (25), we can rewrite c_j in terms of the already computed a_j and b_j :

$$c_j = \frac{1}{d_1^j} \left(a_j k_j(\kappa d_1) + \sum_{m=0}^{\infty} b_m(2j+1)B_{mj}i_j(\kappa d_1) - \frac{q}{4\pi\epsilon_1 d_1} \delta_{0j} \right) \quad (36)$$

Because the charge is located at $r = 0$, only the $n = 0$ terms of Equation (35) will survive, and the potential at this location is:

$$\begin{aligned} \phi_{\text{reac}}(r_1 = 0) &= a_0 k_0(\kappa d_1) + \\ &\sum_{m=0}^{\infty} b_m B_{m0} i_0(\kappa d_1) - \frac{q}{4\pi\epsilon_1 d_1} \end{aligned} \quad (37)$$

The result from Equation (37) in Equation (34) yields the solvation free energy.

For the isolated molecule, $R \rightarrow \infty$ makes $B_{nm} \rightarrow 0$, which nullifies the sum in Equation (37) and a_0 for $R \rightarrow \infty$, from the system in Equation (29), is

$$a_0^\infty = -\frac{q}{d_1^2} \frac{\epsilon_1}{\epsilon_2} \frac{1}{4\pi\kappa k'_0(\kappa d_1)\epsilon_1} \quad (38)$$

Surface free energy with set potential ϕ_0 — We can expand G_p from Equation (14) in Legendre polynomials as

$$G_p = -\frac{\epsilon_2\kappa}{\phi_0} \left[\sum_{n=0}^{\infty} b_n k'_n(\kappa d_2) P_n(\cos \theta_2) + \sum_{n=0}^{\infty} a_n \sum_{m=0}^{\infty} (2m+1) B_{nm} i'_m(\kappa d_2) P_m(\cos \theta_2) \right]. \quad (39)$$

Applying Equation (39) in Equation (14) gives

$$F = 2\pi\kappa\phi_0 d_2^2 \epsilon_2 \left[b_0 k'_0(\kappa d_2) + \sum_{n=0}^{\infty} a_n B_{n0} i'_0(\kappa d_2) \right] \quad (40)$$

If the surface is isolated, $R \rightarrow \infty$ makes $B_{n0} \rightarrow 0$, and the free energy in this case is

$$F = 2\pi\kappa\phi_0 d_2^2 b_0^\infty k'_0(\kappa d_2) \epsilon_2 \quad (41)$$

where b_0^∞ is taken from the system in (29) considering $B_{nm} \rightarrow 0$, which results in

$$b_0^\infty = \frac{\phi_0}{k_0(\kappa d_2)}. \quad (42)$$

Surface free energy with set charge σ_0 — We can expand G_c from Equation (14) in Legendre polynomials as

$$G_c = \frac{1}{\sigma_0} \left[\sum_{n=0}^{\infty} b_n k_n(\kappa d_2) P_n(\cos \theta_2) + \sum_{n=0}^{\infty} a_n \sum_{m=0}^{\infty} (2m+1) B_{nm} i_m(\kappa d_2) P_m(\cos \theta_2) \right] \quad (43)$$

Applying Equation (43) into Equation (14) gives

$$F = 2\pi\sigma_0 d_2^2 \left[b_0 k_0(\kappa d_2) + \sum_{n=0}^{\infty} a_n B_{n0} i_0(\kappa d_2) \right] \quad (44)$$

For the isolated surface, $R \rightarrow \infty$ and $B_{n0} \rightarrow 0$, and the free energy is

$$F = 2\pi\sigma_0 d_2^2 b_0^\infty k_0(\kappa d_2) \quad (45)$$

where b_0^∞ is calculated from the system in (32) considering $B_{nm} \rightarrow 0$, which results in

$$b_0^\infty = -\frac{\sigma_0}{\epsilon_2 \kappa k'_0(\kappa d_2)}. \quad (46)$$

V. RESULTS

To obtain the following results, we extended the **PyGBe** code to consider surfaces with prescribed charge or potential. For most runs, we used a workstation with Intel Xeon X5650 CPUs and one NVIDIA Tesla C2075 GPU card (2011 Fermi). That includes the code verification runs using the analytical solution and the calculations with protein G B1 D4'. The final case considers the antibody immunoglobulin G, which is a much larger molecule than protein G. For these runs, we used Boston University's BUNGEE cluster, which has 16 nodes with 8 Intel Xeon CPU cores each, and a total of 3 NVIDIA Tesla Kepler K20 and 26 NVIDIA Tesla M2070/2075 GPUs. All runs were serial: single-CPU and single-GPU. We used the free **MSMS** software⁴⁴ to generate meshes, and **pdb2pqr**⁴⁵ with an **AMBER** forcefield to determine the charges and van der Waals radii. In these tests, we did not consider a Stern layer for either the protein or the charged surface, nor the presence of solvent-filled cavities inside the protein.

A. Verification against analytical solution

Using the analytical solution detailed in Section IV, we carried out a grid-convergence study of **PyGBe** extended to treat interacting surfaces with biomolecules. The setup consists of a spherical molecule with a 5Å radius and a centered charge of $1e^-$, interacting with a spherical surface of 4Å radius and an imposed potential of $\phi = 1$. The center-to-center distance between the spheres is 12Å, and they are dissolved in water with salt at 145mM, which gives a Debye length of 8 ($\kappa = 0.125$), and permittivity $\epsilon_{\text{sol}} = 80$. The permittivity inside the spherical protein is $\epsilon_{\text{mol}} = 4$. Figure 8 shows a sketch of this system.

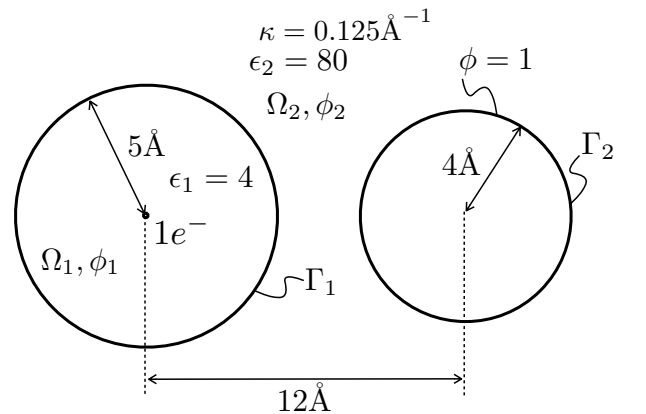


FIG. 8: Sketch of system used in the convergence study of Figure 9.

Figure 9 presents the results of the grid-convergence analysis, where the error is the relative difference in interaction free energy between the analytical result from

Section IV and the numerical solution computed with PyGBe. The observed order of convergence of the three finest meshes was 1.007. Table I presents the numerical parameters used in this case. Recall from section III that we calculate the boundary-element integrals differently for close-by and far-away elements, and use a semi-analytical method for the element that contains the collocation point. The fine Gauss quadrature rule is used for elements closer than $2L$ from the collocation point, where $L = \sqrt{2 \cdot \text{Area}}$. For the treecode, N_{crit} is the maximum number of boundary elements per box, P is the Taylor expansion truncation parameter and θ is the multipole-acceptance criterion. The final numerical parameter is the exit tolerance of the GMRES solver.

TABLE I: Numerical parameters used in the code-verification runs with the analytical solution.

# Gauss points:			Treecode:			GMRES:	
in-element	close-by	far-away	N_{crit}	P	θ	tol.	
9 per side	37	3	300	15	0.5	10^{-9}	

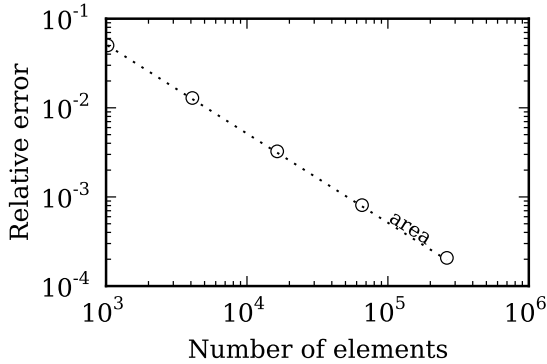


FIG. 9: Grid-convergence study for the interaction free energy between a spherical molecule with a centered charge and a sphere with potential $\phi = 1$. Data sets, figure files plus running/plotting scripts are available under CC-BY.⁴⁶

As seen in Figure 9, the error decays with the average area of the boundary elements ($\frac{1}{N}$), which is the expected behavior considering our previous work.²² This proves that the extension of PyGBe to treat charged surfaces is solving the mathematical model correctly.

B. First case: protein G B1 D4'

We computed the electrostatic field of protein G B1 D4' interacting with a $100\text{\AA} \times 100\text{\AA} \times 10\text{\AA}$ block with surface charge density $\pm 0.05\text{C/m}^2$, and investigated its preferred orientation. The protein was centered with respect to a $100\text{\AA} \times 100\text{\AA}$ face, a distance 2\AA above it. As seen in Figure 4, α_{tilt} is the angle between the protein's dipole moment and the normal vector to the surface, and α_{rot}

rotates about the dipole moment. The dipole-moment vector placed at the center of mass of the protein generates an axis, and we used the line of shortest distance between the outermost atom and this axis as a reference vector \mathbf{V}_{ref} . The rotation angle α_{rot} is the angle between the normal vector to a $100\text{\AA} \times 10\text{\AA}$ side face of the block and \mathbf{V}_{ref} .

In these cases, we considered a solvent with no salt, i.e., $\kappa = 0$ (to compare with other published results), and with relative permittivity 80. The region inside the protein had a relative permittivity of 4.

Grid-convergence study for protein G B1 D4' — By means of a grid-convergence study, we make sure that the runs are in the asymptotic range of the model, select a triangle density so that the geometry is well-resolved by the surface mesh, and find adequate values of the simulation parameters for sampling the orientations. Using Richardson extrapolation, we find values of the energy that estimate the exact solution and use them as a reference to calculate estimated errors. This error is simply the relative difference between the energy obtained numerically with each mesh density and the estimated exact value. In this way, we choose the parameters for the sampling runs with confidence that they are both accurate and efficient in computing time.

We computed the solvation and surface energy of a system containing a surface with charge density 0.05C/m^2 , and a protein at $\alpha_{\text{tilt}} = 10^\circ$ and $\alpha_{\text{rot}} = 200^\circ$. The numerical parameters are presented in Table II. Using runs with mesh densities of 2, 4, and 8 elements per square Angstrom, we obtained the values in Table III using Richardson extrapolation: these are the reference values for the error plotted in Figure 10. The observed order of convergence was 0.96 for the solvation energy and 0.94 for the surface energy. For details on the Richardson-extrapolation method for performing grid-convergence analysis, see our previous work.²³ Figure 10 shows errors that are decaying as $1/N$ in both the solvation and surface energies for the finest three meshes. This indicates that the calculations are in the asymptotic region and the geometry is well resolved in these cases.

TABLE II: Numerical parameters used in the convergence runs with protein G B1 D4'.

# Gauss points:			Treecode:			GMRES:	
in-element	close-by	far-away	N_{crit}	P	θ	tol.	
9 per side	19	7	500	15	0.5	10^{-8}	

TABLE III: Extrapolated values of energy for protein G B1 D4'.

Energy [kcal/mol]	
Solvation	Surface
-222.43	317.98

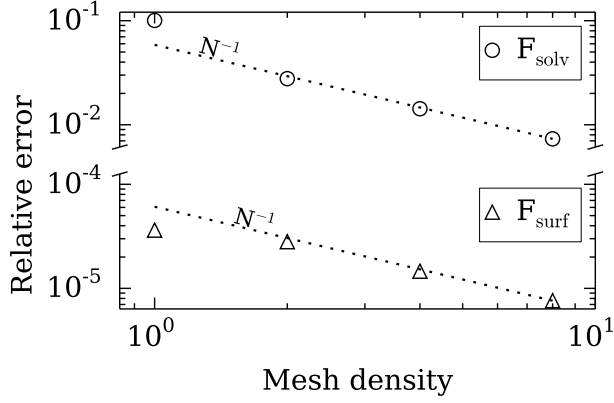


FIG. 10: Grid-convergence study of the solvation and surface energy for protein G B1 D4' mutant, interacting with a surface with a charge density of 0.05C/m^2 . Data sets, figure files and running/plotting scripts available under CC-BY.⁴⁷

Probing orientation of Protein G B1 D4'— We sampled the total free energy every $\Delta\alpha_{\text{tilt}} = 2^\circ$ of tilt angle and $\Delta\alpha_{\text{rot}} = 10^\circ$ of rotation angle, resulting in 3,240 independent runs. The surface mesh had 4 triangles per square Angstrom on the protein geometry and 2 triangles per square Angstrom on the charged surface. Numerical parameters are presented in Table IV.

TABLE IV: Numerical parameters used in the runs probing orientation of protein G B1 D4'.

# Gauss points:			Treecode:			GMRES:	
in-element	close-by	far-away	N_{crit}	P	θ	tol.	
9 per side	19	1	300	4	0.5	10^{-5}	

With total free energy as the input, the integrals of Equation (19) can be computed by means of the trapezoidal rule. Figure 11 presents the probability of the protein orientation in terms of $\cos(\alpha_{\text{tilt}})$, in intervals of $\Delta\cos(\alpha_{\text{tilt}}) = 0.005$ (Fig. 11a) and $\Delta\alpha_{\text{tilt}} = 2^\circ$ (Fig. 11b). Table V presents the average orientation $\langle \cos(\alpha_{\text{tilt}}) \rangle$ for the surface having either positive or negative charge density, and Figure 12 shows the electrostatic potential for the preferred orientation in each case.

TABLE V: Average orientation.

$\langle \cos(\alpha_{\text{tilt}}) \rangle$	
Negative	Positive
-0.968	0.963

C. Second case: immunoglobulin G

We computed the electrostatic field of immunoglobulin G—a protein widely used in biosensors—interacting with a $250\text{\AA} \times 250\text{\AA} \times 10\text{\AA}$ block, varying the conditions of surface charge and salt concentration. The protein was centered with respect to a $250\text{\AA} \times 250\text{\AA}$ face, at a distance 5\AA above it. The solvent had relative permittivity of 80 and the protein of 4.

Grid-convergence study for immunoglobulin G— As in the previous section, we carried out a grid-convergence study to make sure the geometry was well resolved and to find adequate values of the simulation parameters for sampling different orientations. The error in Figure 13 is the relative difference between the energy obtained using PyGBe with each mesh density and the estimated exact value computed with Richardson extrapolation.

In this case, we computed the solvation energy and surface energy of a system consisting of a surface with charge density 0.05C/m^2 and a protein with $\alpha_{\text{tilt}} = 31^\circ$ and $\alpha_{\text{rot}} = 130^\circ$. Using the results from runs with a mesh density of 2, 4, and 8 elements per square Angstrom, we added the solvation and surface energies, and used Richardson extrapolation to obtain a value of -2792.22kcal/mol , and an *observed order of convergence* of 0.85. This is our reference to calculate the errors in Figure 13. There is a slight deviation from the expected value of the observed order of convergence (1.0), which we attribute to the non-uniform mesh generated by msms. Even though the mesh density is on average doubled for each run, there is no guarantee that the refinement is homogeneous throughout the whole molecular surface. The numerical parameters are presented in Table VI.

TABLE VI: Numerical parameters used in the convergence runs with immunoglobulin G.

# Gauss points:			Treecode:			GMRES:	
in-element	close-by	far-away	N_{crit}	P	θ	tol.	
9 per side	19	1	1000	6	0.5	10^{-5}	

Probing orientation of immunoglobulin G— We sampled the total free energy every $\Delta\alpha_{\text{tilt}} = 4^\circ$ of tilt angle and $\Delta\alpha_{\text{rot}} = 20^\circ$ of rotation angle, resulting in a total of 810 runs. The surface meshes had 2 triangles per square Angstrom throughout. Numerical parameters are presented in Table VII.

TABLE VII: Numerical parameters used in the runs probing orientation of immunoglobulin G.

# Gauss points:			Treecode:			GMRES:	
in-element	close-by	far-away	N_{crit}	P	θ	tol.	
9 per side	19	1	300	2	0.5	10^{-4}	

With the computed total free energy, we obtained the probability of each orientation using Equation (19) and

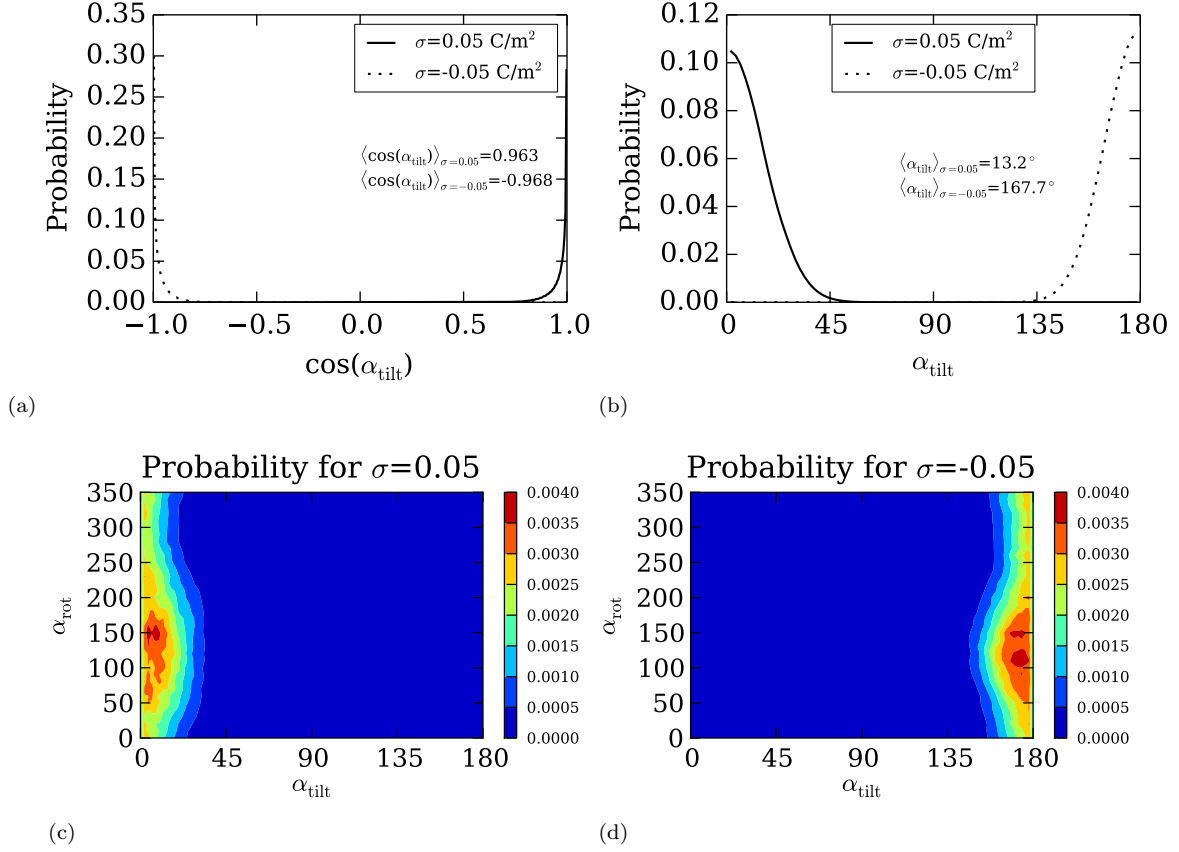


FIG. 11: Orientation probability distribution of protein G B1 D4'. Figures 11a and 11b are the probability with respect to the tilt angle and its cosine, respectively. Figures 11c and 11d are the probability with respect to both the tilt and rotation angle. Data sets, figure files and running/plotting scripts available under CC-BY.⁴⁸

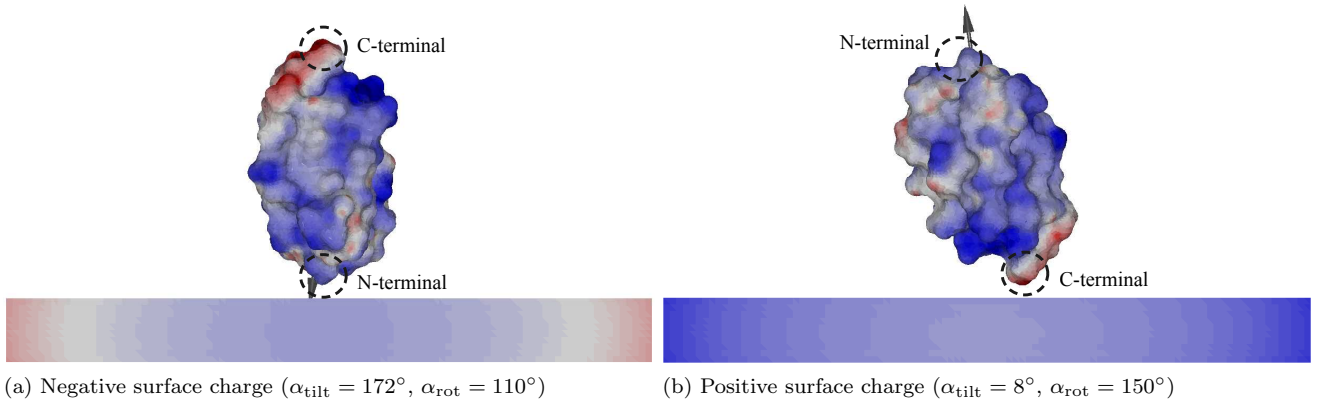


FIG. 12: Electrostatic potential of protein G B1 D4' for the preferred orientations according to Figure 11. Black arrow indicates direction of dipole-moment vector.

the trapezoidal rule. We sampled all combinations with surface charges of $\sigma = \pm 0.05 \text{ C/m}^2$ and $\sigma = \pm 0.2 \text{ C/m}^2$ and salt concentrations of 145mM ($\kappa = 0.125 \text{ \AA}^{-1}$) and 9mM ($\kappa = 0.03125 \text{ \AA}^{-1}$). For each of these cases, Figures 14 and 15 show a color plot of the probability distribution with respect to the tilt and rotation angles, and a 3D plot

of the preferred orientation, where the solvent-excluded surface is colored by the electrostatic potential.

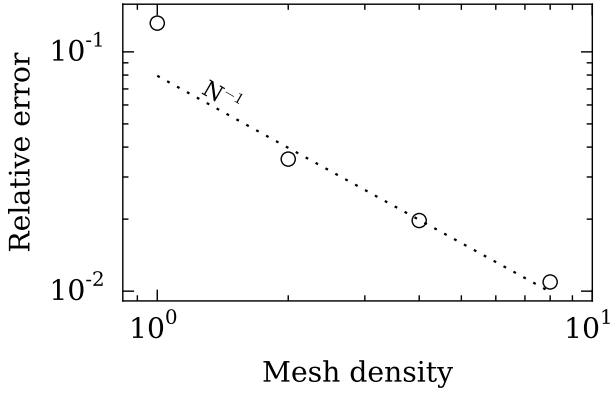


FIG. 13: Grid-convergence study of the solvation plus surface energy for immunoglobulin G interacting with a surface with charge density $0.05\text{C}/\text{m}^2$. Data sets, figure files and plotting scripts available under CC-BY.⁴⁹

D. Reproducibility and data management

We have a consistent reproducibility practice that includes releasing code and data associated with a publication. The **PyGBe** code was released at the time of submitting our previous publication,²³ under an MIT open-source license, and we maintain a version-control repository. As with our previous paper, we also release with this work all of the data needed to run the numerical experiments reported here, including running scripts and post-processing code in Python for producing the figures. To support our open-science goals, we prepared such a “*reproducibility package*” for each of the results presented in Figures 9, 10, 11, 13, and the probability plots in Figures 14 and 15. The included running scripts invoke the **PyGBe** code with the correct input data and meshes (also included), and post-process the results to give the final figure, all with just one command. Please see the respective captions for a reference to the reproducibility packages, hosted on the **figshare** repository.

VI. DISCUSSION

A. Verification with analytical solution

In order to study the interaction of proteins and charged surfaces, we extended **PyGBe** to account for surfaces with prescribed charge or potential. Unfortunately, there was no analytical solution available in the literature to compare and verify **PyGBe**’s extension. Section IV derives a closed expression for a spherical molecule with a centered charge interacting with a spherical surface, and we used this expression to carry out a grid-convergence study of the interaction energy (Figure 9). The error decays with the area, which is the expected behavior^{22,23} for a boundary element method with constant elements. This study verified that **PyGBe** solves the mathematical

model correctly.

Here, the numerical parameters were all chosen for high accuracy because discretization error is very small for a spherical geometry. We wanted to make sure that the errors due to integration, the treecode approximation and the GMRES solver were even smaller. With more realistic molecular geometries, however, discretization errors are larger and accuracy requirements with **PyGBe** are relaxed, resulting in lower runtimes.

B. First case: protein G B1 D4’

The orientation of protein G B1 D4’ near charged surfaces was studied using molecular dynamics (MD) simulations by Liu and co-workers³⁷ and experimentally by Baio and co-workers.³⁸ The availability of these published results was a motivation to test **PyGBe** using this protein.

The results presented in Figure 11 show that for the most likely orientations, the dipole-moment vector is aligned with the vector normal to the interacting surface. This indicates that the dipole moment is the dominant effect that determines the protein’s orientation, over local protein-surface interactions. This result is unsurprising, since protein G B1 D4’ is a relatively small biomolecule.

Moreover, Figure 11 reveals that protein G B1 D4’ behaves like a point dipole, as the most likely orientations shift 180° when the sign of the surface charge is flipped. This is also explained by the dipole moment dominating the orientation.

The dipolar behavior described by our calculations with **PyGBe** agrees with the experiments done by Baio and co-workers,³⁸ in which they observed opposite orientations of protein G B1 D4’ adsorbed on NH_3^+ and COO^- self-assembled monolayers. With positively charged surfaces, most of the proteins oriented with the N-terminal of the protein pointing away from the surface, while for negatively charged surfaces the opposite occurred, with the C-terminal pointing away from the surface. This agrees with our results in Figure 11 since the dipole moment vector of protein G B1 D4’ points from the C-terminal to the N-terminal.

Liu and co-workers³⁷ used MD simulations to obtain $\langle \cos(\alpha_{\text{tilt}}) \rangle = 0.95$ for $\sigma = 0.05\text{C}/\text{m}^2$, and $\langle \cos(\alpha_{\text{tilt}}) \rangle = -0.85 \pm 0.05$ for $\sigma = -0.05\text{C}/\text{m}^2$, which agrees well with our results in Table V. MD simulations consider van der Waals interactions and conformational changes of the protein, whereas these are not considered in our approach, explaining the slight differences in $\langle \cos(\alpha_{\text{tilt}}) \rangle$.

C. Second case: immunoglobulin G

With the extension of **PyGBe** verified with an analytical solution (Section VIA) and confirmation that the implicit-solvent model can be used to study protein-surface interaction with a small protein (Section VIB),

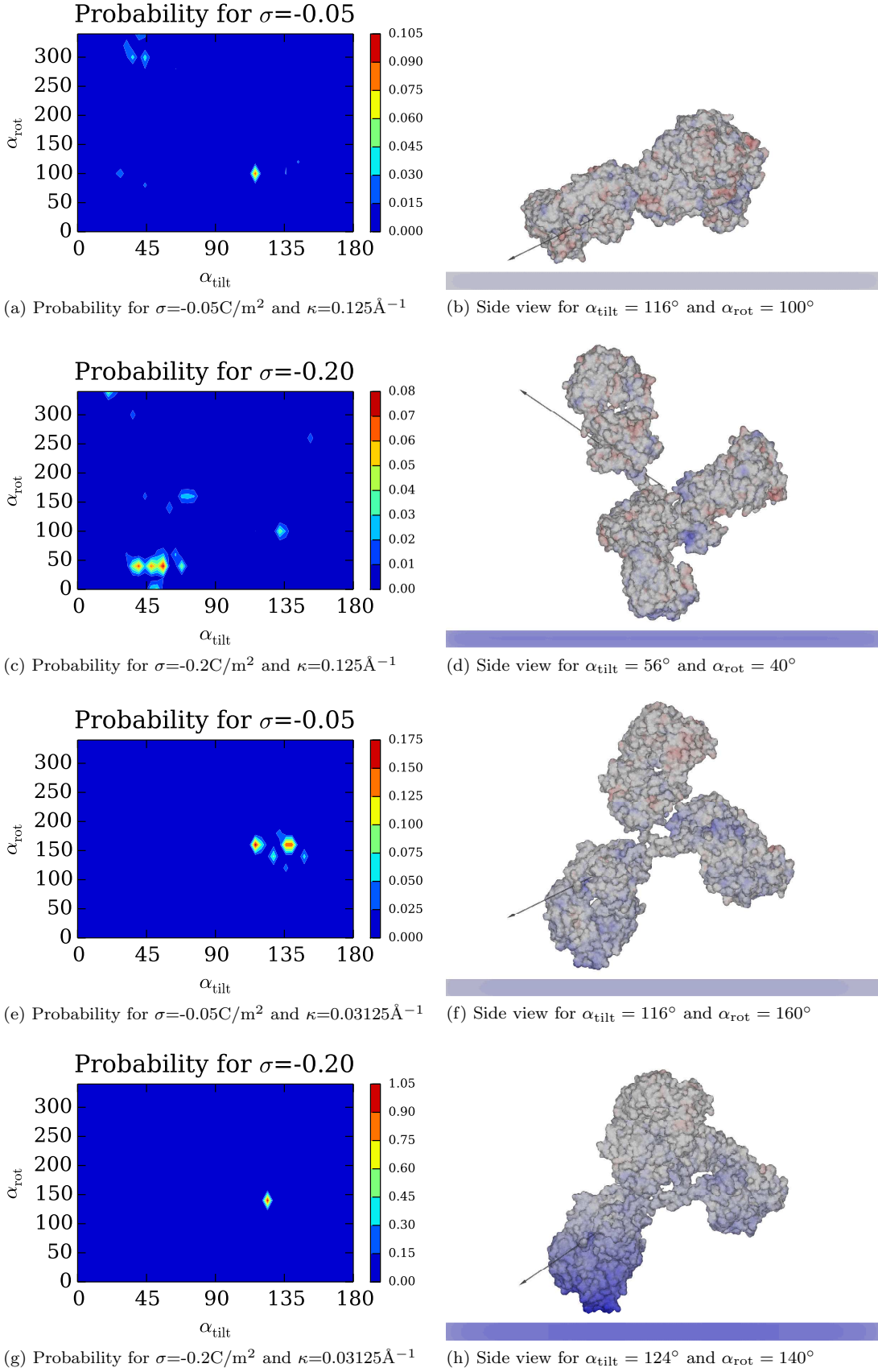


FIG. 14: Orientation probability distribution and surface potential of the preferred orientation for immunoglobulin G near a negative surface charge. The black arrow indicates the direction of the dipole moment. Data sets, figure files and plotting scripts available under CC-BY.⁴⁹

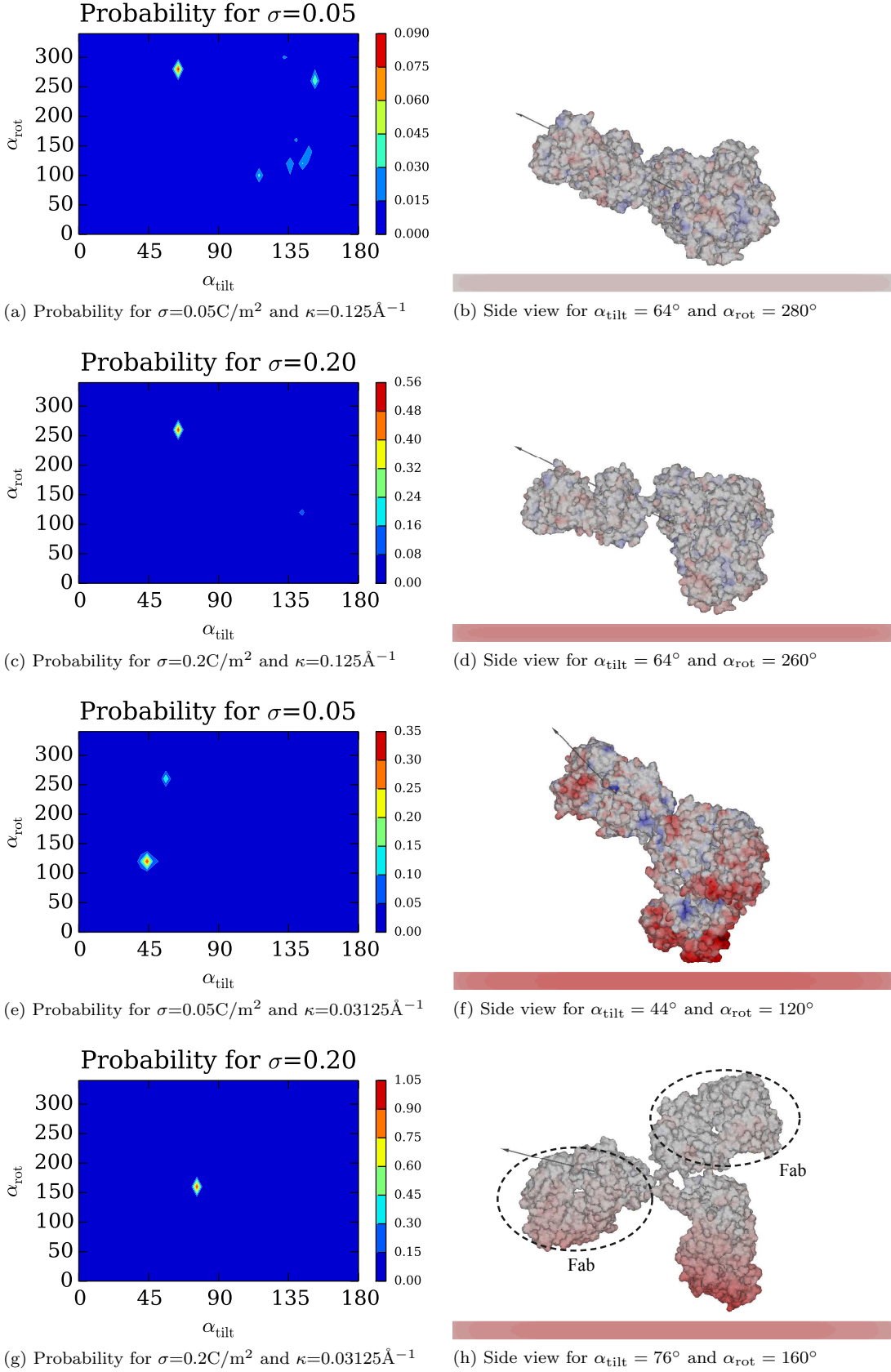


FIG. 15: Orientation probability distribution and surface potential of the preferred orientation for Immunoglobulin G near a positive surface charge. The black arrow indicates the direction of the dipole moment. Data sets, figure files and plotting scripts available under CC-BY.⁴⁹

we proceeded to explore the effect of surface charge and salt concentration on the orientation of the antibody immunoglobulin G. Antibodies are widely used in biosensors as ligand molecules, due to their affinity and specificity with the target molecule (antigen), and it is vitally important that they are adsorbed on the sensor with the fragment antigen-binding (Fab) pointing away from the sensor, into the incoming flow containing the antigens.

Figures 14 and 15 present the probability distribution of immunoglobulin G for many orientations (given by α_{tilt} and α_{rot}) varying the surface charge (σ) and salt concentration (κ). Figures 14a and 15a show that for low surface charge ($\sigma \pm 0.05\text{C/m}^2$) and high salt concentration ($\kappa = 0.125\text{\AA}^{-1}$), there is no clear preferred orientation, to the point that the most likely orientation has a probability of around 10%. This means that adsorbing the antibodies under these conditions would result in a wide range of orientations, which is not favorable for biosensor fabrication.

Effect of surface charge— With greater surface charge, in this case $\sigma = \pm 0.2\text{C/m}^2$, the orientation probability distribution gets narrower for positive surface charge, and is maintained for negative surface charge. Figure 15c shows a much clearer preferred orientation, with a probability more than $5\times$ higher for positive surface charge at high salt concentration. For low salt concentrations (Figures 14g and 15g), this effect is even larger.

The results presented on Figures 14 and 15 also show that increasing the surface charge has very little effect on the dipole moment orientation. This is evidence that, in contrast to the case of protein G B1 D4', local interactions dominate over the dipole moment. If the dipole moment were the dominant effect, the dipole moment vector would tend to align to the surface normal as the surface charge increases.

Effect of salt concentration— We also varied the Debye length (κ^{-1}) four-fold. In terms of salt concentration, it means a $16\times$ decrease in the amount of salt.

Like increasing the surface charge, lowering the salt concentration narrows the orientation probability distribution. For $\sigma = \pm 0.05\text{C/m}^2$ (Fig. 14e and Fig. 15e), the effect on positive or negative surface charge is very similar: the preferred orientation is about $2\times$ more likely. However, for $\sigma = \pm 0.2\text{C/m}^2$, the increase is larger with negative surface charge (Fig. 14g), than with positive surface charge (Fig. 15g). The narrower probability distribution is explained by the lower shielding effect caused by the reduced salt content, which at the same time increases the electrostatic interaction.

From the results in Figure 14 and Figure 15, we can conclude that it is easier to control the antibody orientation with low salt concentration and high surface charge, because the orientation probability distribution is the narrowest. In our results, Figures 14h and 15h show the orientation of the antibody at the lowest salt concentration and higher surface charge, but only the orientation

in Figure 15h, with positive surface charge, is favorable for biosensing applications, since the Fab fragments are pointing up.

That favorable orientations for biosensing applications are best obtained with high positive surface charge and low salt concentration is consistent with experimental observations by Chen and co-workers.⁵⁰ These researchers developed a coarse-grained method known as the united residue model,¹⁸ which qualitatively aligns with our results.

VII. CONCLUSION

In this work, we successfully used an implicit-solvent model to study protein orientation near charged surfaces. We present for the first time and apply an extension of our open-source **PyGBe** code to account for the presence of charged surfaces. The new feature of the code was verified against an analytical solution, which we derived for that purpose.

Using **PyGBe**, we obtained that protein G B1 D4' behaves like a point dipole near a charged surface, with the dipole-moment vector shifting $\sim 180^\circ$ when the sign of the surface charge flips. Our results compare well with experimental observations and simulations using molecular dynamics, supporting the use of our approach for probing protein orientation near charged surfaces. We applied our approach to immunoglobulin G, a biomolecule that is much larger than protein G B1 (about $125\times$, by volume) and would be challenging to study via molecular dynamics. Through this study, we realized that this protein is best immobilized on a surface with positive charge, for example with a NH_3^+ self-assembled monolayer, using high surface charge and low salt concentration.

We conclude that this implicit-solvent model can offer a valuable approach in biosensor studies. In this application, ligand molecules undergo little conformational change as they adsorb on the sensor surface, and thus the assumption of a rigid structure is valid. In our future work, we intend to use this approach to aid the design of better ligand molecules, by looking at the orientation for different ligand molecule mutants.

ACKNOWLEDGMENTS

This work was supported by ONR via grant #N00014-11-1-0356 of the Applied Computational Analysis Program. LAB also acknowledges support from NSF CAREER award OCI-1149784 and from NVIDIA, Inc. via the CUDA Fellows Program. We are grateful for many helpful conversations with members of the Materials and Sensors Branch of the Naval Research Laboratory, especially Dr. Jeff M. Byers and Dr. Marc Raphael.

¹Jeffrey J. Gray, "The interaction of proteins with solid surfaces," *Curr. Opin. Struct. Biol.* **14**, 110–115 (2004).

- ²Michael Rabe, Dorinel Verdes, and Stefan Seeger, "Understanding protein adsorption phenomena at solid surfaces," *Adv. Colloid Interface Sci.* **162**, 87–106 (2011).
- ³Ju-Young Byun, Yong-Beom Shin, Taihua Li, Jin-Ho Park, Dong-Myung Kim, Dong-Hwan Choi, and Min-Gon Kim, "The use of an engineered single chain variable fragment in a localized surface plasmon resonance method for analysis of the c-reactive protein," *Chem. Commun.* **49**, 9497–9499 (2013).
- ⁴Anke K. Trilling, Tamara Hesselink, Adèle van Houwelingen, Jan H. G. Cordewener, Maarten A. Jongsma, Sanne Schoffelen, Jan C. M. van Hest, Han Zuilhof, and Jules Beekwilder, "Orientation of llama antibodies strongly increases sensitivity of biosensors," *Biosens. Bioelectron.* **60**, 130–136 (2014).
- ⁵Nobuyuki Tajima, Madoka Takai, and Kazuhiko Ishihara, "Significance of antibody orientation unraveled: Well-oriented antibodies recorded high binding affinity," *Anal. Chem.* **83**, 1969–1976 (2011).
- ⁶Anke K. Trilling, Jules Beekwilder, and Han Zuilhof, "Antibody orientation on biosensor surfaces: a minireview," *Analyst* **138**, 1619–1627 (2013).
- ⁷B. Roux and T. Simonson, "Implicit solvent models," *Biophys. Chem.* **78**, 1–20 (1999).
- ⁸Jaydeep P. Bardhan, "Biomolecular electrostatics — I want your solvation (model)," *Comput. Sci. Disc.* **5** (2012).
- ⁹B. J. Yoon and A. M. Lenhoff, "Computation of the electrostatic interaction energy between a protein and a charged surface," *J. Phys. Chem.* **96**, 3130–3134 (1992).
- ¹⁰Charles M. Roth and Abraham M. Lenhoff, "Electrostatic and van der Waals contributions to protein adsorption: computation of equilibrium constants," *Langmuir* **9**, 962–972 (1993).
- ¹¹Dilipkumar Asthagiri and Abraham M. Lenhoff, "Influence of structural details in modeling electrostatically driven protein adsorption," *Langmuir* **13**, 6761–6768 (1997).
- ¹²Yan Yao and Abraham M. Lenhoff, "Electrostatic contributions to protein retention in ion-exchange chromatography. 1. cytochrome c variants," *Anal. Chem.* **76**, 6743–6752 (2004).
- ¹³Yan Yao and Abraham M. Lenhoff, "Electrostatic contributions to protein retention in ion-exchange chromatography. 2. proteins with various degrees of structural differences," *Anal. Chem.* **77**, 2157–2165 (2005).
- ¹⁴Charles M. Roth, Brian L. Neal, and Abraham M. Lenhoff, "Van der Waals interactions involving proteins," *Biophys. J.* **70**, 977–987 (1996).
- ¹⁵Yu-Jane Sheng, Heng-Kwong Tsao, Jian Zhou, and Shaoyi Jiang, "Orientation of a Y-shaped biomolecule adsorbed on a charged surface," *Phys. Rev. E* **66** (2002).
- ¹⁶Jian Zhou, Heng-Kwong Tsao, Yu-Jane Sheng, and Shaoyi Jiang, "Monte Carlo simulations of antibody adsorption and orientation on charged surfaces," *J. Chem. Phys.* **121**, 1050–1057 (2004).
- ¹⁷Alexander S. Freed and Steven M. Cramer, "Protein-surface interaction maps for ion-exchange chromatography," *Langmuir* **27**, 3561–3568 (2011).
- ¹⁸Jian Zhou, Shengfu Chen, and Shaoyi Jiang, "Orientation of adsorbed antibodies on charged surfaces by computer simulation based on a united-residue model," *Langmuir* **19**, 3472–3478 (2003).
- ¹⁹P. Maarten Biesheuvel, Marijn van der Veen, and William Norde, "A modified Poisson-Boltzmann model including charge regulation for the adsorption of ionizable polyelectrolytes to charged interfaces, applied to lysozyme adsorption on silica," *J. Phys. Chem. B* **109**, 4172–4180 (2005).
- ²⁰Rune A. Hartvig, Marco van de Weert, Jesper Ostergaard, Lene Jorgensen, and Henrik Jensen, "Protein adsorption at charged surfaces: The role of electrostatic interactions and interfacial charge regulation," *Langmuir* **27**, 2634–2643 (2011).
- ²¹<https://github.com/barbagroup/pygbe>.
- ²²Christopher D. Cooper and L. A. Barba, "Validation of the PyGBe code for Poisson-Boltzmann equation with boundary element methods," Technical Report on **figshare**, CC-BY license, doi:10.6084/m9.figshare.154331 (January 25 2013).
- ²³Christopher D. Cooper, Jaydeep P. Bardhan, and L. A. Barba, "A biomolecular electrostatics solver using Python, GPUs and boundary elements that can handle solvent-filled cavities and Stern layers," *Comput. Phys. Commun.* **185**, 720–729 (March 2014), preprint on arXiv:1309.4018.
- ²⁴B. J. Yoon and A. M. Lenhoff, "A boundary element method for molecular electrostatics with electrolyte effects," *J. Comput. Chem.* **11**, 1080–1086 (1990).
- ²⁵A. H. Juffer, E. F. F. Botta, B. A. M. Vankeulen, A. Vanderploeg, and H. J. C. Berendsen, "The electric potential of a macromolecule in a solvent: A fundamental approach," *Journal of Computational Physics* **97**, 144–171 (1991).
- ²⁶B. Lu, X. Cheng, J. Huang, and J. A. McCammon, "Order N algorithm for computation of electrostatic interactions in biomolecular systems," *P. Natl. Acad. Sci. USA* **103**, 19314–19319 (2006).
- ²⁷C. Bajaj, S. C. Chen, and A. Rand, "An efficient higher-order fast multipole boundary element solution for Poisson-Boltzmann-based molecular electrostatics," *SIAM J. Sci. Comput.* **33**, 826–848 (2011).
- ²⁸M. D. Altman, J. P. Bardhan, J. K. White, and B. Tidor, "Accurate solution of multi-region continuum electrostatic problems using the linearized Poisson-Boltzmann equation and curved boundary elements," *J. Comput. Chem.* **30**, 132–153 (2009).
- ²⁹W. H. Geng and R. Krasny, "A treecode-accelerated boundary integral poisson-boltzmann solver for solvated biomolecules," *J. Comp. Phys.* **247**, 62–78 (2013).
- ³⁰Z. Zhu, J. Huang, B. Song, and J. White, "Improving the robustness of a surface integral formulation for wideband impedance extraction of 3D structures," in *Proceedings of the 2001 IEEE/ACM Int. Conf. on Computer-Aided Design* (2001) pp. 592–597.
- ³¹L. Greengard and V. Rokhlin, "A fast algorithm for particle simulations," *J. Comput. Phys.* **73**, 325–348 (1987).
- ³²J. Barnes and P. Hut, "A hierarchical $O(N \log N)$ force-calculation algorithm," *Nature* **324**, 446–449 (December 1986).
- ³³J. R. Phillips and J. K. White, "A precorrected-FFT method for electrostatic analysis of complicated 3-D structures," *IEEE Trans. Comput. Aid. D.* **16**, 1059–1072 (1997).
- ³⁴P. Li, H. Johnston, and R. Krasny, "A Cartesian treecode for screened Coulomb interactions," *J. Comp. Phys.* **228**, 3858–3868 (2009).
- ³⁵Derek Y. Chan and D. John Mitchell, "The free energy of an electrical double layer," *J. of Coll. and Inter. Science* **95**, 193–197 (1983).
- ³⁶Steven L. Carnie and Derek Y. Chan, "Interaction free energy between identical spherical colloidal particles: The linearized poisson-boltzmann theory," *J. of Coll. and Inter. Science* **155**, 297–312 (1993).
- ³⁷Jie Liu, Chenyi Liao, and Jian Zhou, "Multiscale simulations of protein G B1 adsorbed on charged self-assembled monolayers," *Langmuir* **29**, 11366–11374 (2013).
- ³⁸Joe E. Baio, Tobias Weidner, Loren Baugh, Lara J. Gamble, Patrick S. Stayton, and David G. Castner, "Probing the orientation of electrostatically immobilized protein g b1 by time-of-flight secondary ion spectrometry, sum frequency generation, and near-edge x-ray adsorption fine structure spectroscopy," *Langmuir* **28**, 2107–2112 (2012).
- ³⁹N. Guex and M. C. Peitsch, "SWISS-MODEL and the Swiss-PdbViewer: An environment for comparative protein modeling," *Electrophoresis* **18**, 2714–2723 (1997).
- ⁴⁰<http://www.expasy.org/spdbv/>.
- ⁴¹Steven L. Carnie, Derek Y. Chan, and James S. Gunning, "Electrical double layer interaction between dissimilar spherical colloidal particles and between a sphere and a plate: The linearized poisson-boltzmann theory," *Langmuir* **10**, 2993–3009 (1994).
- ⁴²Itay Lotan and Teresa Head-Gordon, "An analytical electrostatic model for salt screened interactions between multiple proteins," *J. Chem. Theory Comput.* **2**, 541–555 (2006).
- ⁴³Stjepan Marcelja, D. John Mitchell, Barry W. Ninham, and Michael J. Sculley, "Role of solvent structure in solution theory,"

- J. Chem. Soc. Faraday II **73**, 630–648 (1977).
- ⁴⁴Michel F Sanner, Arthur J Olson, and Jean-Claude Spehner, “Fast and robust computation of molecular surfaces,” in *Proceedings of the eleventh annual symposium on Computational geometry* (ACM, 1995) pp. 406–407.
- ⁴⁵T. J. Dolinsky, J. E. Nielsen, J. A. McCammon, and N. A. Baker, “PDB2PQR: an automated pipeline for the setup of Poisson–Boltzmann electrostatics calculations,” *Nucleic Acids Research* **32**, W665–W667 (2004).
- ⁴⁶Christopher D. Cooper and L. A. Barba, “Grid convergence of PyGBe with a spherical molecule near spherical surface,” Data, figures and plottings script on **figshare**, CC-BY license, <http://dx.doi.org/10.6084/m9.figshare.1348841> (March 2015).
- ⁴⁷Christopher D. Cooper and L. A. Barba, “Grid convergence of PyGBe with protein G B1 D4,” Data, figures and plottings script on **figshare**, CC-BY license, <http://dx.doi.org/10.6084/m9.figshare.1348803> (March 2015).
- ⁴⁸Christopher D. Cooper and L. A. Barba, “Protein orientation near a charged surface using PyGBe and protein G B1 D4,” Data, figures and plottings script on **figshare**, CC-BY license, <http://dx.doi.org/10.6084/m9.figshare.1348804> (March 2015).
- ⁴⁹Christopher D. Cooper and L. A. Barba, “Grid convergence of PyGBe with immunoglobulin G near a charged surface,” Data, figures and plottings script on **figshare**, CC-BY license, <http://dx.doi.org/10.6084/m9.figshare.1348801> (March 2015).
- ⁵⁰Shengfu Chen, Lingyun Liu, Jian Zhou, and Shaoyi Jiang, “Controlling antibody orientation on charged self assembled-monolayers,” *Langmuir* **19**, 2859–2864 (2003).